# SYNOPTIC Hα FULL-DISK OBSERVATIONS OF THE SUN FROM BIG BEAR SOLAR OBSERVATORY

## I. *Instrumentation, Image Processing, Data Products, and First Results*

C. DENKER[1], A. JOHANNESSON[1], W. MARQUETTE[1], P. R. GOODE[1], H. WANG[1]
and H. ZIRIN[2]

[1] *Big Bear Solar Observatory, New Jersey Institute of Technology, 40386 North Shore Lane,
Big Bear City, CA 92314, U.S.A.*
[2] *California Institute of Technology, 264-33 Caltech, Pasadena, CA 91125, U.S.A.*

**Abstract.** The Big Bear Solar Observatory (BBSO) has a long tradition of synoptic full-disk observations. Synoptic observations of contrast enhanced full-disk images in the Ca II K-line have been used with great success to reproduce the H I Lα irradiance variability observed with the Upper Atmosphere Research Satellite (UARS). Recent improvements in data calibration procedures and image-processing techniques enable us now to provide contrast enhanced Hα full-disk images with a spatial resolution of approximately $2''$ and a temporal resolution of up to 3 frames min$^{-1}$.

In this first paper in a series, we describe the instruments, the data calibration procedures, and the image-processing techniques used to obtain our daily Hα full-disk observations. We also present the final data products such as low- and high-contrast images, and Carrington rotation charts. A time series of an erupting mini-filament further illustrates the quality of our Hα full-disk observations and motivate one of the future research projects. This lays a solid foundation for our subsequent studies of solar activity and chromospheric fine structures. The high quality and the sunrise-to-sunset operation of the Hα full-disk observations presented in this paper make them an ideal choice to study statistical properties of mini-filament eruptions, chromospheric differential rotation, and meridional flows within the chromosphere, as well as the evolution of active regions, filaments, flares, and prominences.

## 1. Introduction

Synoptic Hα full-disk images are provided by many observatories around the world, e.g., Holloman Air Force Base in New Mexico, Kiepenheuer Institut für Sonnenphysik at the Observatorio del Teide/Tenerife in Spain, Learmonth Solar Observatory in Australia, National Solar Observatory at Sacramento Peak in New Mexico, Sonnenobservatorium Kanzelhöhe in Austria, and Hα spectroheliograms from Observatoire de Paris Meudon in France. In the past, high-resolution Hα imaging could only be carried out on limited areas of the Sun. Modern, large-format CCD cameras enable us to obtain detailed images of the whole Sun. To the best of our knowledge, the only other large-format CCD camera used for Hα full-disk observations is operated at the Hiraiso Solar Terrestrial Research Center in Japan (Akioka, 1996). In this paper, we report on new image-processing techniques enhancing the contrast of all chromospheric features and make limb prominences visible, as well.

Hα full-disk observations were usually used to survey solar activity, to find interesting objects, and to monitor flares. However, there are only a few research projects based on Hα full-disk observations alone, and we argue that large-format CCD cameras and advanced image-processing techniques provide a unique opportunity for studies with full-disk data.

Full-disk data from BBSO have been mainly analyzed in the context of irradiance variations with the solar cycle, e.g., high-contrast, full-disk images observed in the Ca II K-line were successfully used in previous studies (Johannesson, Marquette, and Zirin, 1995, 1997) to reproduce the H I Lα irradiance variability observed with the Upper Atmosphere Research Satellite (UARS) and to model the extreme ultraviolet irradiance variability of the Sun (Warren *et al.*, 1996). Lean *et al.* (1998) utilized BBSO's contrast-enhanced Ca K filtergrams to assess the component of solar irradiance variability that can be attributed to bright magnetic features. We refined the data acquisition and image-processing techniques and applied them to white-light and Hα full-disk images in October 1997. Currently, we are investigating the potential of supplementary observations in the G-band at 430.6 nm and in the violet wavelength region from 382.8 nm to 384.6 nm where many absorption lines are formed by Mg I, Fe I, and CN molecules (Chapman, 1970).

With the *Yohkoh* satellite, the Solar and Heliospheric Observatory (SOHO) and the Transition Region and Coronal Explorer (TRACE) in space probing the solar atmosphere from the photosphere to the corona, Hα full-disk observations with high temporal and spatial resolution should prove to be one of the key diagnostic tools for determining the magnetic field topology between the photosphere, transition region, and corona. Domingo, Fleck, and Poland (1995) presented an overview of the SOHO mission, and first results from SOHO have been published in a special issue of *Solar Physics* (Fleck, 1997). The TRACE mission was outlined in Strong *et al.* (1994).

We first show a typical contrast-enhanced Hα full-disk image which was observed on 29 October 1997. In the following sections, we will focus on this particular data set to demonstrate and examine its potential to study solar activity and the evolution of chromospheric fine structures. Figure 1 shows an Hα full-disk image superimposed on a Stonyhurst grid. Several dark filaments and two active regions (NOAA 8099 and NOAA 8100) with bright Hα plages are visible in this contrast-enhanced image. The image calibration and image-processing procedures described in this paper allow the simultaneous display of disk features, as well as prominences above the solar limb. The richness in detail of these limb features is at least comparable or even better than observations made with complex instruments such as the Hα coronagraph at the Observatoire du Pic du Midi in France (Niot and Noëns, 1997). Studying prominences and corresponding filaments at the same time, which is only one of the advantages of our high-contrast images, provides deeper insight into their temporal evolution and their supporting magnetic
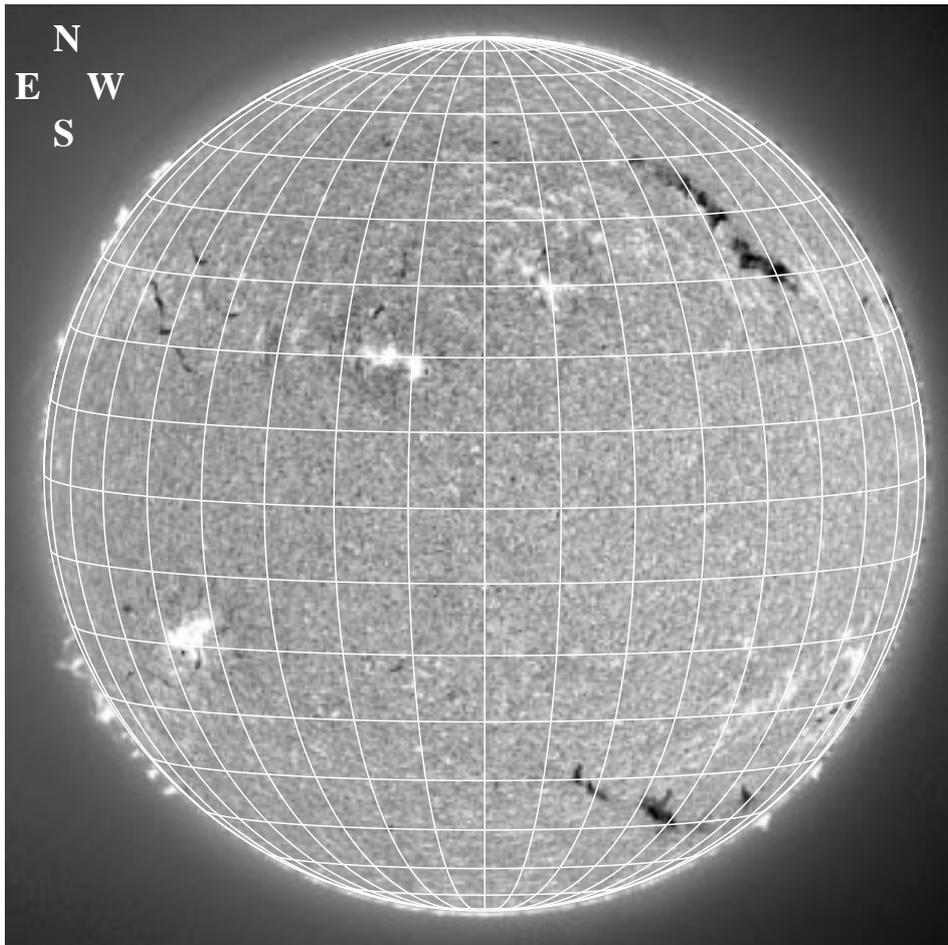
*Figure 1.* BBSO synoptic Hα full-disk image observed on 29 October 1997. This image has been processed to remove limb darkening and to enhance contrast which alllows the simultaneous display of disk features and limb prominences.

field configuration, especially in combination with simultaneous observations of sensitive magnetograms.

In forthcoming papers, we will focus on statistical properties of mini-filament eruptions, differential rotation and meridional flows within the chromosphere, and the evolution of active regions with a special emphasis on new flux emergence, filaments, and prominences. At the end of this paper, we present a few preliminary results which outline the series of papers about to be published.

## 2. Instrumentation

### 2.1. SINGER FULL-DISK TELESCOPE

The full-disk telescope at BBSO was built as part of the astronaut training program for *Skylab*. The most recent optical set-up of the Singer telescope is shown in Figure 2. A singlet lens $L_1$ of 22.4 cm diameter and focal length of 233.4 cm is used to collimate the light. The singlet is aspherically ground to correct for spherical aberration and coated to transmit a broad (30 nm) band centered on H$\alpha$. The singlet lens is used to minimize thermal focus changes during observing runs. Similarly, all optical elements are mounted on Invar rods which run through the telescope. The camera is mounted at the rear on a rotating mount so that P-angle changes can be compensated. The telescope has its own guider so that it can be operated independently from the 65 cm vacuum reflector and 25 cm vacuum refractor sharing the same equatorial mount. The telescope was built by Boller and Chivens under contract to the Link Division of Singer-General Precision in Binghamton, New York. Hence the name Singer Telescope. In the original configuration, the Singer telescope was evacuated and an internally reflecting Fabry–Pérot was used for the H$\alpha$ full-disk observations recorded with a precision Photo-sonic film camera. In 1985, we switched to a Lyot filter. The revised optical set-up is shown in Figure 2. Because the primary image size is about 22 mm and the aperture of the Halle filter (0.05 nm bandpass) is 29 mm, the full image could pass through the filter, but it was necessary to introduce a weak field lens $L_2$ just ahead of the filter to image the pupil on the 210 mm focal length Schneider Componon lens $L_3$ used to relay the image to the camera. This gives an 18 mm image at the final focus. Because it would have been difficult to operate the Halle filter in vacuum, we decided to omit the vacuum and, as we have found with other small aperture refractors, no significant change in the performance was noted. Further, the aperture was decreased to 15 cm to fit the Halle filter. The overall telescope is now considerably longer than needed, but we avoided expensive mechanical modifications. In 1996 we were able to purchase a large format Kodak 4.2 CCD camera to replace the out-of-date film system. The diffraction limit at $\lambda = 656.3$ nm for a 15 cm telescope is, according to the Rayleigh criterion, $\alpha = 1.22\,\lambda/D = 1.1''$ and the image scale is approximately $1''$ pixel$^{-1}$, i.e., the full-disk images are under-sampled by a factor of approximately 2. However, the system is well adapted to the seeing conditions at the site with typical Fried-parameters $r_0$ around 8 cm (Denker and Wang, 1998).

### 2.2. DETECTOR AND DATA ACQUISITION

The detector used for data acquisition is a solid-state charge coupled device (CCD), full-frame imager KAF-4200 made by KODAK. The sensor of this Kodak Megaplus Model 4.2 CCD camera provides an array of 2032 (horizontal) $\times$ 2028 (vertical) pixel. Each pixel is 9 $\mu$m $\times$ 9 $\mu$m and has a 100% fill factor for complete light sensitivity and extremely accurate two-dimensional measurements. The dimension
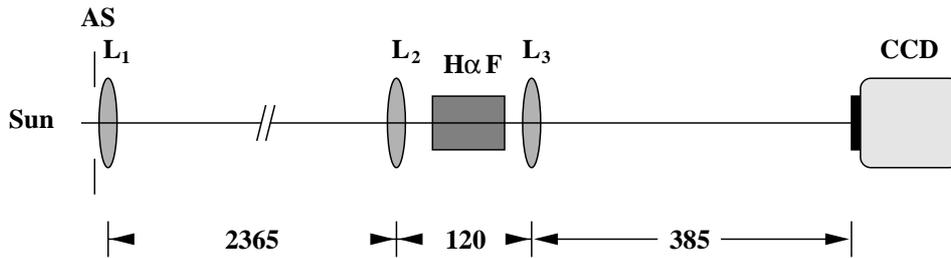
*Figure 2.* Optical set-up of the Hα full-disk telescope. AS: aperture stop, $L_1$: coated 22.4 cm singlet lens, $L_2$: weak field lens, HαF: Halle Hα filter, $L_3$: Schneider Componon relay lens $L_3$, and CCD: Kodak 4.2 CCD camera. The distances are given in millimeters.

of the image sensor is 18.5 mm × 18.5 mm. The pixel clock rate of the Kodak 4.2 camera is 10 MHz and the images are digitized with 8-bit accuracy. The maximum frame rate amounts to 2.1 frames $s^{-1}$. The dynamic range of the sensor is greater than 65 dB at the input of the A/D converter. The maximum spectral response of the sensor is around 600 nm. The exposure times are variable in the range from 1 ms to several seconds. The response time of the mechanical shutter is in the order of 15 ms which causes a noticeable variation of the light level at the sensor for exposure times below 15 ms.

The CCD camera is operated by a Power Computing PowerWave 133 using a PowerPC 604e under MacOS 8.1 running at 132 MHz with 64 MByte RAM. Two additional output channels of the Perceptics imaging board are interfaced to an electronic switch so that two additional Kodak Megaplus cameras can be controlled at the same time. The data are stored on a 1 GByte Iomega Jaz-disk that can be exchanged very quickly to allow continued observations eventhough the Jaz-disk is repeatedly filled up. At the end of the day, the data are burned on CD-ROMs which are archived at BBSO.

## 3. Image Processing

In this section, we will discuss the various image-processing steps as summarized in the block diagram shown in Figure 3. The first panel, 'Input Data', of the block diagram refers to the image acquisition which was described in detail in the previous section. The control computer for the Kodak 4.2 CCD camera is connected via the standard File Transfer Protocol (FTP) to a 300 MHz Pentium II personal computer operating under Linux. The image-processing tool is written in the Interactive Data Language (IDL) from Research Systems, Inc. providing the observers with an intuitive Graphical User Interface (GUI) to monitor the different steps of the image processing described below. Finally, the data are published via the World Wide Web (WWW) and archived on CD-ROM. Usually, it takes about 30 min to obtain, process, and display the images on the WWW. The outstanding continuity
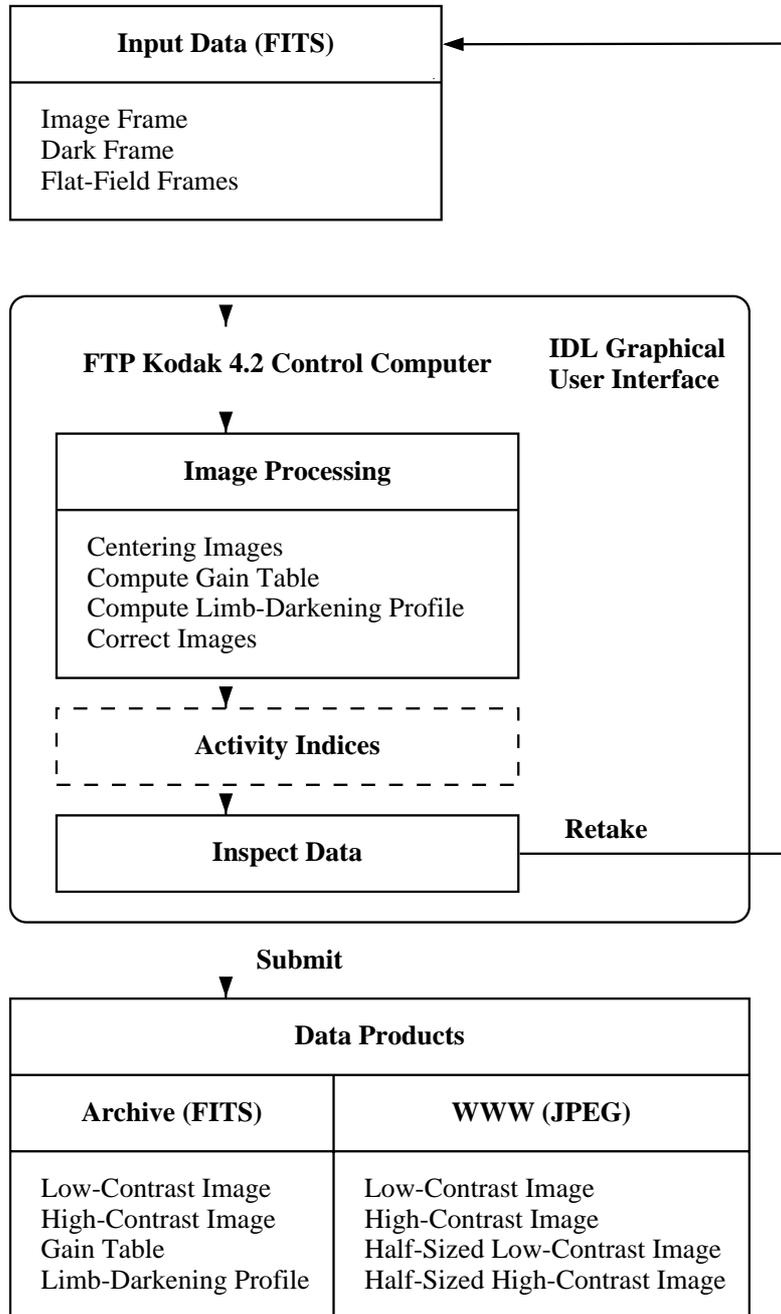
| Input Data (FITS) |
| :--- |
| Image Frame |
| Dark Frame |
| Flat-Field Frames |

**FTP Kodak 4.2 Control Computer**        **IDL Graphical User Interface**

| Image Processing |
| :--- |
| Centering Images |
| Compute Gain Table |
| Compute Limb-Darkening Profile |
| Correct Images |

| Activity Indices |
| :--- |

| Inspect Data |        **Retake**

**Submit**

| Data Products | |
| :--- | :--- |
| **Archive (FITS)** | **WWW (JPEG)** |
| Low-Contrast Image | Low-Contrast Image |
| High-Contrast Image | High-Contrast Image |
| Gain Table | Half-Sized Low-Contrast Image |
| Limb-Darkening Profile | Half-Sized High-Contrast Image |

*Figure 3.* Block diagram of image acquisition and image processing.

of Hα full-disk observations and the excellent seeing conditions at BBSO, as recent seeing tests by the National Solar Observatory demonstrate (Beckers, 1997), make this data set most valuable for solar physics and space weather studies. One of the most important task is for example to study and monitor flares. Especially during solar maximum when several flare-producing active regions are present, it is crucial to measure their individual contribution to the overall solar activity. The next sub-sections contain a comprehensive description of image and gain table calibration, an accurate scheme to center the full-disk images, and the computation of the two-dimensional limb darkening function.

## 3.1. NOISE CHARACTERISTICS

A typical set of calibration frames consists of a dark frame and seven flat-field frames. Depending on sky brightness and solar activity, the exposure times range from 20 to 35 ms. A typical exposure time is about 30 ms. The exposure time of the calibration frames and full-disk images is usually the same during the daily observing run. Since the Kodak 4.2 CCD camera is not cooled, temperature variations throughout the day can change the average dark signal. To test the stability of the dark signal, we took a time series of 82 dark frames separated by 10 min. The dark variation, mostly due to the slowly rising ambient temperatures, was about 0.03 counts per hour, and should be negligible for the further data analysis. The average dark signal varies between 2.5 and 3.0 counts resulting in only a minor shrinking of the camera's dynamic range. Therefore, cooling the camera would not result in a significantly larger dynamic range. The only benefit to cooling would be a stabilized dark signal which is of minor importance due to the very small overall temperature drift of 0.03 counts $hr^{-1}$ and the small frame to frame variations of around 0.07 counts.

We derived the read-out noise by subtracting several consecutive dark frames and computed the corresponding frequency distribution of the differences. The frequency distribution is a Gaussian $f(x) = \exp(-(x - \mu)^2/2\sigma^2)$ centered at $\mu = 0$ counts and $\sigma_d$ amounts to 0.58 counts. The frequency distribution for several consecutive frames on a fixed target with approximately the same illumination level as the Hα full disk frames is again a Gaussian with $\sigma_f = 0.95$ counts. This gives an estimate for the photon noise of $\sigma_{ph} = 0.37$ which is slightly less than the read-out noise. Since photometric studies are not the primary goal of our full-disk observations, the noise statistics are probably of minor importance. However, if we study features above the solar limb such as prominences, the estimates for read-out and photon noise establish the threshold above which faint fine structure become discernible at the disk edge. We measured the stray-light level from an average limb intensity profile. The stray-light level at $100''$ outside the limb amounts to 3.8% of the disk center brightness. We chose a distance of $100''$ to avoid falsifying contributions from prominences. Without stray-light correction, the faintest structures of prominences show only 10 to 15% of the intensity at disk center.
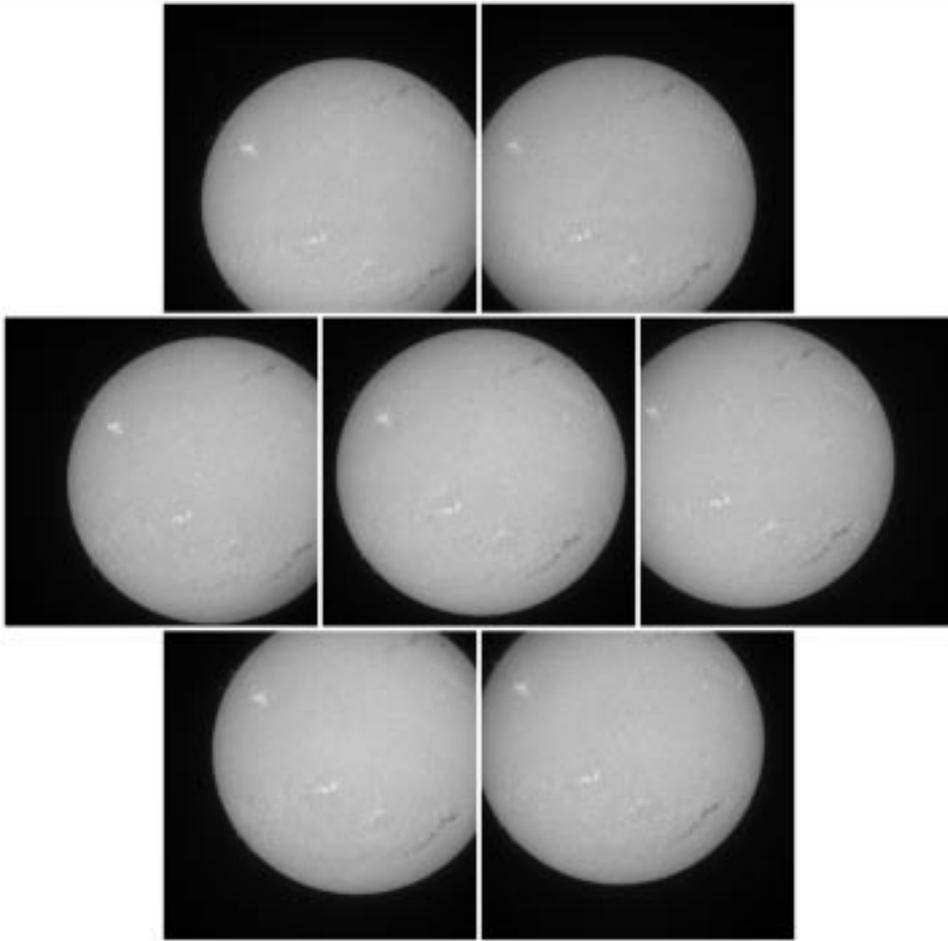
*Figure 4.* Input frames for the flat-fielding procedure. The solar disk is centered in one frame and shifted around on the detector in the other frames.

### 3.2. GAIN TABLE CALIBRATION

The flat-field frames were obtained while off-pointing the telescope from Sun center. Figure 4 shows a typical set of frames that were used to derive a flat-field frame. The calibration frames and a few Hα full-disk images are stored with the Flexible Image Transport System (FITS, NOST 1991), whereas the remainder of the images have to be stored in the compressed Joint Photographic Experts Group (JPEG) format to save disk space. The size of a FITS image is approximately 4 MByte, whereas the average size of a JPEG image is approximately 0.4 MByte. On a typical observing day (8 hours) and with two full-disk images per minute, approximately 400 MByte are obtained even with data compression. The rms error introduced by the JPEG data compression is about 0.7% of the mean solar intensity

which is typically in the range between 150 and 190 counts. This error has to be accounted for in photometric studies. JPEG compression preserves the shape of the Hα fine structure, however, the compression algorithm can create a typical $8 \times 8$ pixel sized pattern which results in artificial boundaries in feature identification schemes, i.e., the full-disk images have to be smoothed before applying feature tracking techniques.

We use an improved version of the Kuhn–Lin method (Kuhn, Lin, and Loranz, 1991) to compute the gain table for all BBSO synoptic full-disk observations (white-light, Ca II K-line, G-band, and Hα). Their method is particularly useful for full-disk observations, since it utilizes only image data to derive the gain table, and does not require a large number of image frames to average out solar features or defocusing the telescope which changes the light path and therefore yields an incorrect gain table. The basic idea of the Kuhn–Lin technique for calibrating spatially non-uniform image array detectors is to compute the horizontal and vertical derivatives of the logarithm of the gain function from multiple displaced full-disk images. Once the gradient of the log-gain function is determined, integration of this function leads to the logarithm of the gain within an additive constant, i.e., the gain is determined within an overall multiplicative factor. Finally, an iterative least-square algorithm is used to solve the pixel gain function for various displacement vectors. The accuracy of the Kuhn–Lin technique and its practical limitations such as seeing variations, sky brightness variations, and non-linear shutter responses are discussed in detail in Kuhn, Lin, and Loranz (1991). Figure 4 shows a typical set of frames that is used as input for the Kuhn–Lin algorithm. Computing the gain table from the full-sized flat-field frames would take too long. Therefore, we reduce the size of the calibration frames, which were corrected for the dark frame, by a factor of 8 to $254 \times 253$ pixels before running the flat-fielding procedure. The resulting miniature gain table is subsequently enlarged to original frame size. Since the pixel-to-pixel gain variation is only computed where displacement vectors are defined, there will be regions on the detector, especially in the corners, without any information about the gain. To cover these areas, we extrapolate the gain table progressively from the inner part to the edges.

Figure 5(a) shows a gain table derived with the Kuhn–Lin method. The rms-contrast of the pixel-to-pixel variation amounts to 6.7% for the full gain table and to 3.5% for the central part of the gain table that is used to image the Sun. The vignetting, interference fringes, and non-uniformities of the Lyot filter, clearly discernible in this figure, have been successfully removed from the high contrast image shown in Figure 1. Without proper gain table calibration, these features will cause serious artifacts in the limb darkening corrected images and, consequently, problems would arise for automatic feature identification and local correlation tracking or feature tracking techniques – all primary objectives of our synoptic full-disk program.
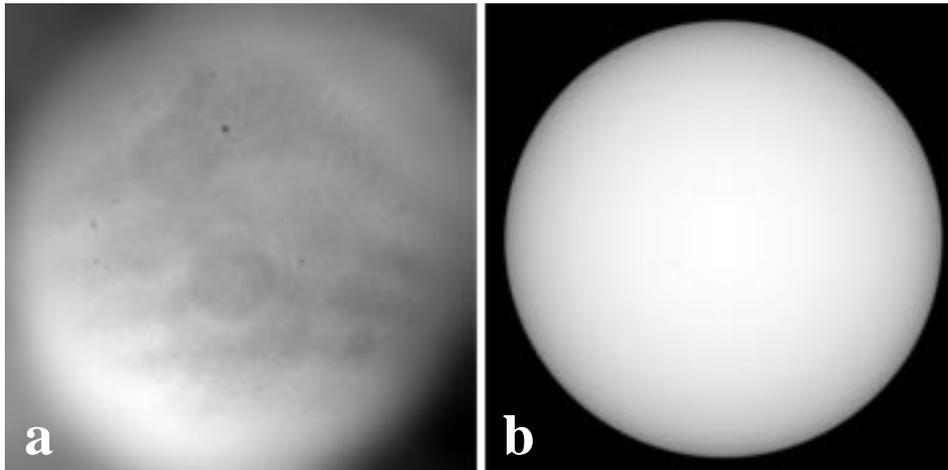
*Figure 5.* (a) Gain table derived with the Kuhn–Lin technique and (b) two-dimensional limb darkening function.

### 3.3. CENTERING THE FULL-DISK IMAGES

Determining the center coordinates of the solar disk with an accuracy of one pixel or less is a difficult task, especially in the case of Hα full-disk images where prominences extend above the limb and disk features possess high contrast. As a first approximation, we can use an edge detection operator such as the non-linear Sobel function. Since the solar limb has a steep gradient, we can create, by means of a suitable threshold, a mask in which pixels outlining the solar limb (and some pixels inside the limb) are set to unity and all the remaining pixels are set to zero. Searching for the first and last pixel set to unity in $x$- and $y$-direction yields the solar diameter in east–west (E–W) and north–south (N–S) direction and the center coordinates of the solar disk. Once the solar diameter is known, we can use the same algorithm to measure the displacement vectors between the off-center frames that were used in the flat-fielding procedure. Since even small offsets between the two dimensional limb darkening function and the flat-field corrected full disk image will result in a bright and dark aureole on opposite edges of the full-disk image, the centering algorithm will need further refinement.

We select four rectangular regions centered at the E, W, N, and S limb. The size of these regions is $60'' \times 120''$ with the long sides of the rectangle parallel to the solar limb. Next, we compute the four corresponding average limb profiles. To find the center coordinate in E–W direction, we reverse the W limb profile and compute the absolute differences between the E and W profile by shifting the E along the W profile. The minimum of the absolute differences gives a correction for the first approximation of the E–W center coordinate. Analogously, we repeat the procedure for the N–S direction. The absolute difference method finds the center coordinates and determines the solar diameter with an accuracy of one pixel or less.
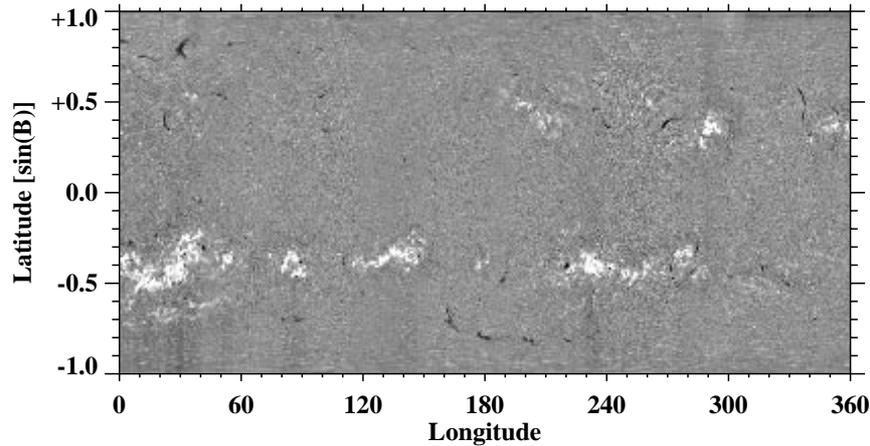
*Figure 6.* Synoptic chart of Hα full-disk images for Carrington rotation 1934.

## 3.4. LIMB DARKENING PROFILE

First, the disk center brightness is derived from a $200'' \times 200''$ area at disk center. We use the median of the intensity at disk center, since it is less sensitive to asymmetric intensity distributions than the mean value. An asymmetric intensity distribution originates from bright Hα plages in active regions or from dark filaments. The disk center brightness for the 29 October 1997 data amounts to 177 counts. Second, a bilinear interpolation algorithm is used to translate the Hα full-disk images from Cartesian coordinates to polar coordinates resulting in one radial disk profile per $1°$ in azimuth. Computing the median value at each radial position yields an average radial profile. We used the median for the same reasons mentioned above. In addition, if fewer than 10 pixels exceed 1.5 times the disk center brightness, we discard them before computing the median. Third, a second order least-squares polynomial fit to the average disk profile is used to replace the inner 25% of the average disk profile. The average disk profile is further smoothed by means of a floating average using wider smoothing kernels at the flatter part of the profile at disk center. Finally, the smoothed average disk profile is linearly interpolated onto a two-dimensional Cartesian grid and the missing points outside the disk are filled in with the lowest value of the disk profile. The two-dimensional limb-darkening function is shown in Figure 5(b).

## 4. First Results

The first results from contrast-enhanced Hα full-disk images are synoptic charts for each Carrington rotation. The entire surface of the Sun is re-mapped into longitude measured from the central meridian and latitude. The re-mapped images are shifted to the corresponding Carrington longitude and merged together with the data from
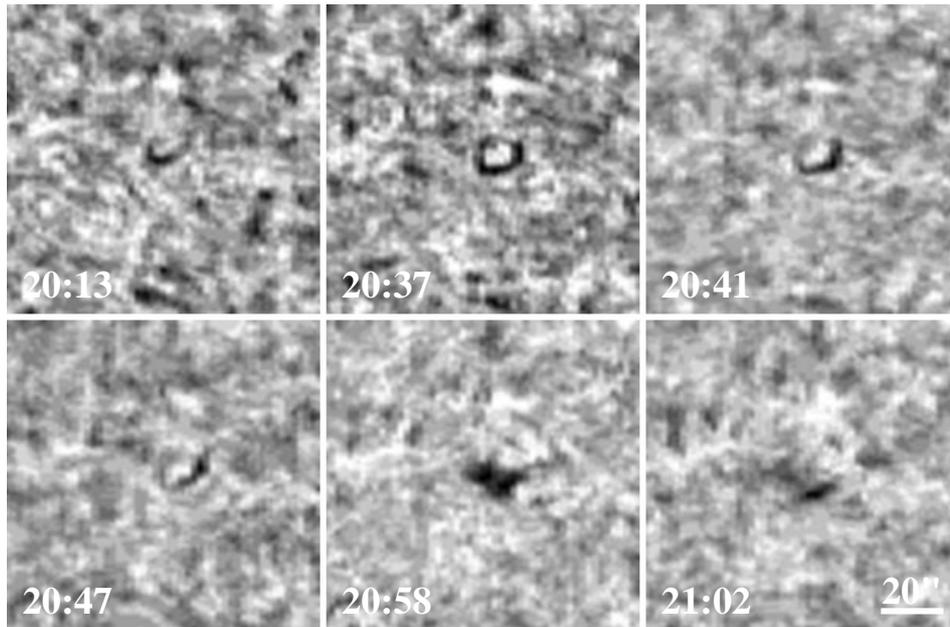
*Figure 7.* Temporal evolution of an erupting mini-filament observed at disk center on 29 October 1997 from 20:13 to 21:02 UT. The field of view for the individual images is $100'' \times 100''$.

previous observing days. Data gaps can be filled in by observations from preceding or following days as long as the center of the image is less than 40° away from the missing Carrington longitude. In Figure 6, we show an example of a synoptic chart for Carrington rotation 1934. Note the very pronounced asymmetry of the bright Hα plages between the northern and southern hemisphere which is a very interesting characteristic of the rising phase of the new solar cycle No. 23. In the next paragraphs, we will change the focus from this global point of view of solar activity to the much smaller scale of erupting mini-filaments.

The first detailed description of mini-filaments was given by LaBonte (1979) who, however, subsumed them into the classification of macrospicules. Hermans and Martin (1986) pointed out that mini-filament eruptions are the small scale analog to large scale filament eruptions. Mini-filaments are a typical manifestation of magnetic activity on the quiet Sun. The energy release and mass ejection of erupting mini-filaments is of particular importance since both can contribute to coronal heating and solar wind acceleration due to the large number of these events. The advantage of daily high-contrast Hα full-disk images is obvious: the position of mini-filaments, and therefore their spatial distribution, is easy to measure. In addition, we can follow temporal variations of their surface density and spatial distribution so that we can address for example the question whether their occurrence is correlated with coronal holes or not. With contrast-enhanced full-disk images in hand, detailed studies of individual erupting mini-filaments and their temporal

evolution with time scales of a minute or less are possible as demonstrated in Figure 7. An MPEG movie of this erupting mini-filament is shown on the World Wide Web at: `http://www.bbso.njit.edu/movies.html`.

The mini-filament in Figure 7 was observed near disk center on 29 October 1997. Since we observed the mini-filament close to disk center, we do not have to consider geometrical foreshortening. We noticed it for the first time shortly after 20:10 UT. The mini-filament started as a dark arch-like structure as shown at the center of the first panel in Figure 7 at 20:13 UT. It subsequently increased in both area and absorption, and its shape resembled more and more that of an almost closed circle. The diameter of the circle was slightly smaller than $20''$. The end of the pre-eruption phase is characterized by strong proper motions along the ring-like mini-filament. In this process, the filament at the left footpoint almost disappears whereas the absorption at the other footpoint increases. The maximum of the increased absorption is reached at 20:41 UT but the proper motion along the filament continues until the filament is barely visible at 20:50 UT. Immediately after this, the mini-filament breaks open at its top ejecting a fuzzy cloud of absorbing material. The cloud is ejected toward the lower left corner until its remnants fades away. The last panel of Figure 7 at 21:02 UT shows the final stage of the mini-filament. The lifetime of this particular mini-filament was approximately one hour and the ejection phase lasted less than 10 min. In a forthcoming paper, we will present a detailed investigation of mini-filament morphology, temporal evolution, statistical properties, and energy/mass distribution.

The prominence, filament, and active region shown in Figure 8 give an impression of the fine structure visible in the Hα full-disk images. Even faint threads are discernible in Figure 8(a) (cf., Niot and Noëns, 1997), and proper motions along individual barbs of a filament in Figure 8(b) are easily to trace in time lapse movies. One of the ongoing research projects at BBSO is to understand the correlation between filament/prominence disapperances and coronal mass ejections (CMEs) and to study their possible driving mechanisms, e.g., a statistical study of filament disappearances during the period of September 1991 through September 1994 is given by Wang *et al.* (1998). However, most observations failed to establish a systematic correlation among the onset of solar flares, filament/prominence eruptions, and CMEs (Harrison, 1995; McAllister, 1996). One of the difficulties in establishing a possible relationship between filament eruptions and CMEs is that CMEs are more likely to be detected if they are limb events, while filament eruptions are more easily visible as disk events. Any search for a correlation between filament eruptions and CMEs needs to be able to consider both disk and limb CMEs and the attendant phenomena.

To present an overview of solar activity, we provide a miniature movie of Hα images for the last 30 observing days on the WWW which allows for example a quick look analysis of the temporal evolution of active regions such as NOAA 8099 shown in Figure 8(c).
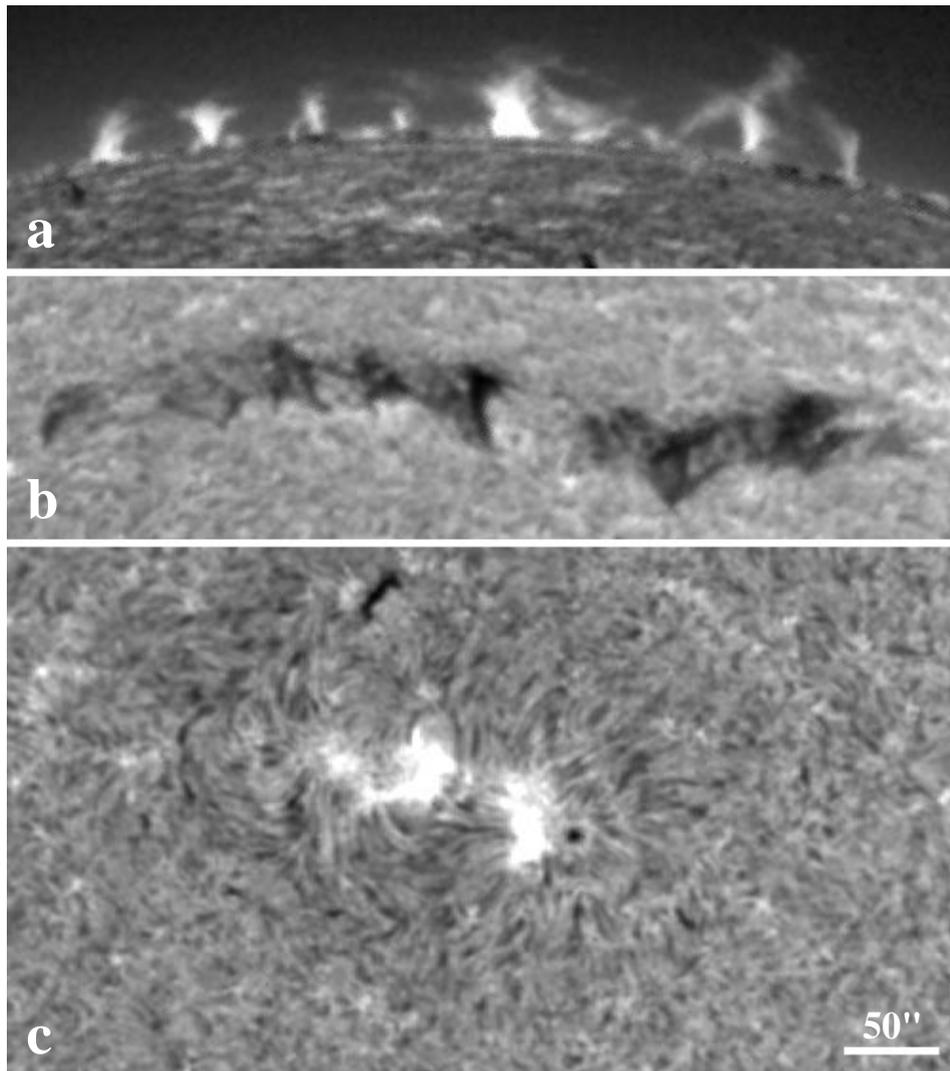
*Figure 8.* Detail study of (a) a prominence, (b) a filament, and (c) active region NOAA 8099.

Until now, Hα full-disk images depicting solar flares were normally saturated because the exposure times were set to a constant value and optimized to yield high-contrast images of the quiet Sun. The bright flaring regions were therefore over-exposed. Since the Hα intensity gives a minimum temperature for the flare region, it is important to obtain proper photometric data even when the full-disk brightness is suddenly rising during a flare. While the Kodak 4.2 CCD camera has only an 8-bit dynamic range, an automatic software control has been implemented in the camera control software which permits the accurate evaluation of flare brightness. The temporal evolution of a M7 flare is shown in Figure 9 during
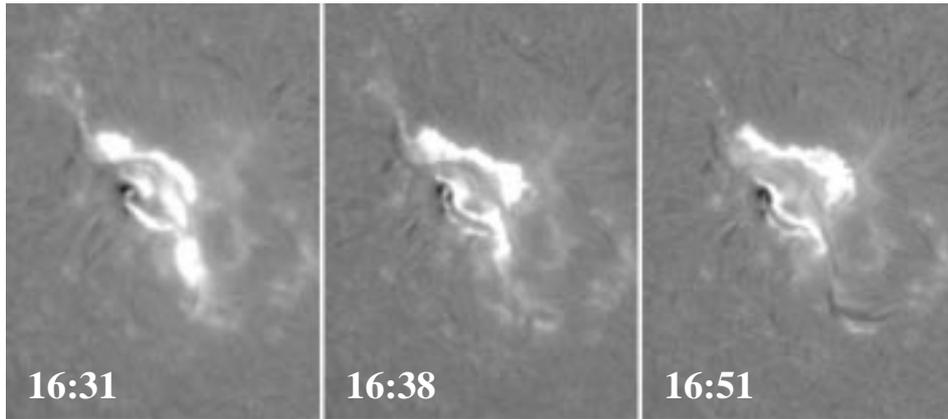
*Figure 9.* Temporal evolution of an M7 flare during its maximum phase in active region NOAA 8210 observed on 29 April 1998. The field of view of the individual frames amounts to $300'' \times 400''$. The images are $\gamma$-corrected to enhance the details in the background.

its maximum phase from 16:31 to 16:51 UT on 29 April 1998. NOAA 8210 was a very active flare-producing region with two X-class and several M-class flares during its disk passage. New emerging positive polarity flux merged with the main negative sunspot creating a $\delta$-configuration (opposite polarity umbrae within a common penumbra).

## 5. Prospects and Summary

In this first paper of a series, we presented a detailed description of the synoptic Hα full-disk observing program at Big Bear Solar Observatory. The quality, as well as the temporal and spatial resolution of the contrast enhanced Hα full-disk images make them an ideal tool to study solar activity from small-scale mini-filaments up to large complex active regions. We believe that our efforts to provide state-of-the-art, ground-based full-disk observations will produce many new and interesting results, especially during the period of time where the *Yohkoh*, SOHO, and TRACE missions are in space studying the solar atmosphere.

In the second half of 1998, we will implement a new camera control system that will enable us to perform the synoptic Hα full-disk observations independently from the operation of our other two Kodak CCD cameras. The enhanced performance of the new imaging board and a faster computer will allow us to further increase the frame rate. Since the diffraction limit at $\lambda = 656.3$ nm for a 22.4 cm telescope is according to the Rayleigh criterion $\alpha = 1.22\,\lambda/D = 0.74''$, it might be worthwhile in the future to remove the aperture stop at the entrance of the telescope and opening the first singlet lens $L_1$ to full aperture. We are considering a larger format CCD camera, as well. With a large-format $4000 \times 4000$ pixels CCD camera it will be possible to observe Hα full-disk images with $1''$ spatial resolu-

tion. However, seeing effects will become more important since such a system will require longer exposure times. Another drawback are the large computer demands to handle and process $4000 \times 4000$ pixel images. We intend to explore the potential of high-resolution ($0.5''$ pixel$^{-1}$) full-disk images in the near future.

Daily H$\alpha$ full-disk images of Big Bear Solar Observatory are published via the WWW at `http://www.bbso.njit.edu/`. The synoptic H$\alpha$ full-disk data is accessible via anonymous FTP at `ftp://ftp.bbso.njit.edu/pub/fulldisk/halpha/`.

## Acknowledgements

## References

Akioka, M.: 1996, *J. Geomag. Geoelectr.* **48**, 5.

Beckers, J.: 1997, *Bull. Am. Astron. Soc.* **29/2**, 897.

Chapman, G. A.: 1970, *Solar Phys.* **13**, 78.

Denker, C. and Wang, H.: 1998, *Astrophys. J.* **502**, 493.

Domingo, V., Fleck, B., and Poland, A. I.: 1995, *Solar Phys.* **162**, 1.

Fleck, B.: 1997, *The First Results from SOHO*, *Solar Phys.* **170/1**.

Harrison, R. A.: 1995, *Astron. Astrophys.* **304**, 585.

Hermans, L. M. and Martin, S. F.: 1986, in A. I. Poland (ed.), *Coronal and Prominence Plasmas*, NASA Conf. Publ. 2442, p. 369.

Johannesson, A., Marquette, W., and Zirin, H.: 1998, *Solar Phys.* **177**, 265.

Johannesson, A., Marquette, W., and Zirin, H.: 1995, *Solar Phys.* **161**, 201.

Kuhn, J. R., Lin, H., and Loranz, D.: 1991, *Publ. Astron. Soc. Pac.* **103**, 1097.

LaBonte, B. J.: 1979, *Solar Phys.* **61**, 283.

Lean, J. L., Cook, J., Marquette, W., and Johannesson, A.: 1998, *Astrophys. J.* **492**, 390.

McAllister, A. H., Dryer, M., McIntosh, P., Singer, H., and Weiss, L.: 1996, *J. Geophys. Res.* **101**, 13.

Niot, J. M. and Noëns, J. C.: 1997, *Solar Phys.* **173**, 53.

NOST: 1991, *Implementation of the Flexible Image Transport System (FITS)*. NASA/OSSA, Goddard Space Flight Center, Greenbelt.

Strong, K., Bruner, M., Tarbell, T., Title, A., and Wolfson, C. J.: 1994, *Space Sci. Rev.* **70**, 119.

Wang, H., Komenda, A., Tang, F., and Zirin, H.: 1998, *Solar Phys.* **178**, 109.

Warren, H. P., Mariska, J. T., Lean, J., Marquette, W., and Johannesson, A.: 1996, *Geophys. Res. Lett.* **23**, 2207.